ACS APPLIED MATERIALS & INTERFACES

www.acsami.org Research Article

Doping- and Strain-Dependent Electrolyte-Gate-Induced Perovskite to Brownmillerite Transformation in Epitaxial $La_{1-x}Sr_xCoO_{3-\delta}$ Films

Vipul Chaturvedi, William M. Postiglione, Rohan D. Chakraborty, Biqiong Yu, Wojciech Tabiś, Sajna Hameed, Nikolaos Biniskos, Andrew Jacobson, Zhan Zhang, Hua Zhou, Martin Greven, Vivian E. Ferry, and Chris Leighton*

Cite This: *ACS Appl. Mater. Interfaces* 2021, 13, 51205−51217 Read Online

ACCESS | Metrics & More | Article Recommendations | Supporting Information

Downloaded via UNIV OF MINNESOTA on May 2, 2022 at 19:31:24 (UTC).
See https://pubs.acs.org/sharingguidelines for options on how to legitimately share published articles.

ABSTRACT: Much recent attention has focused on the voltage-driven reversible topotactic transformation between the ferromagnetic metallic perovskite (P) $SrCoO_{3-\delta}$ and oxygen-vacancy-ordered antiferromagnetic insulating brownmillerite (BM) $SrCoO_{2.5}$. This is emerging as a paradigmatic example of the power of electrochemical gating (using, *e.g.*, ionic liquids/gels), the wide modulation of electronic, magnetic, and optical properties generating clear application potential. $SrCoO_3$ films are challenging with respect to stability, however, and there has been little exploration of alternate compositions. Here, we present the first study of ion-gel-gating-induced P → BM transformations across almost the entire $La_{1-x}Sr_xCoO_3$ phase diagram ($0 \leq x \leq 0.70$), under both tensile and compressive epitaxial strain. Electronic transport, magnetometry, and *operando* synchrotron X-ray diffraction establish that voltage-induced P → BM transformations are possible at essentially all x, including $x \leq 0.50$, where both P and BM phases are highly stable. Under small compressive strain, the transformation threshold voltage decreases from approximately +2.7 V at $x = 0$ to negligible at $x = 0.70$. Both larger compressive strain and tensile strain induce further threshold voltage lowering, particularly at low x. The P → BM threshold voltage is thus *tunable*, *via* both composition and strain. At $x = 0.50$, voltage-controlled ferromagnetism, transport, and optical transmittance are then demonstrated, achieving Curie temperature and resistivity modulations of ~220 K and at least 5 orders of magnitude, respectively, and enabling estimation of the voltage-dependent Co valence. The results are analyzed in the context of doping- and strain-dependent oxygen vacancy formation energies and diffusion coefficients, establishing that it is thermodynamic factors, not kinetics, that underpin the decrease in the threshold voltage with x, that is, with increasing formal Co valence. These findings substantially advance the practical and mechanistic understanding of this voltage-driven transformation, with fundamental and technological implications.

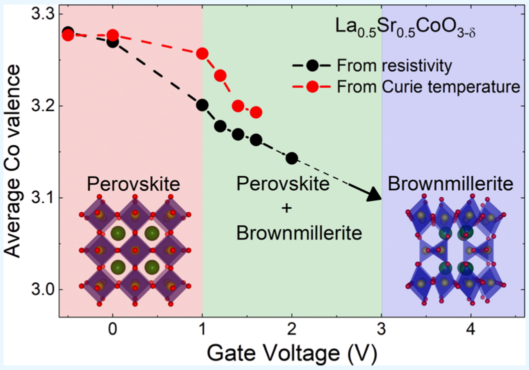

KEYWORDS: *electrolyte gating, ionic control of materials, perovskite oxides, cobaltites, voltage-controlled magnetism*

1. INTRODUCTION

The general concept of electrochemical control of materials has gained substantial traction recently, driven by both fundamental and applied interest.[1−9] Electrochemical transistor-type devices have been formed by interfacing ionic liquids, ion gels (ionic liquid−polymer composites), ionic conductors, or solid electrolytes with target materials, using ionic motion under a gate voltage (V_g) to actuate interfacial electrochemistry in the target material, thus controlling properties.[1−9] Such approaches have realized notable successes, including voltage control of magnetism and transport, the latter encompassing insulator−metal transitions, semiconducting transport, superconductivity, and thermal transport.[1−9] Oxides have proven to be ideal targets for this approach; electrochemical reduction enables electron doping or hole compensation *via* oxygen vacancy (V_O) formation, with reversal of V_g enabling reoxidation *via* V_O annihilation.[1,2,4,5,7−9] Electrolysis of residual H_2O in electrolytes likely plays a key role in such processes,[1−12] providing an oxygen reservoir for reoxidation of the oxide.

Electrochemical control of the cobaltite $SrCoO_{3-\delta}$ (SCO) is emerging as a paradigmatic example of the power of this approach.[1,11−20] Perovskite (P) $SrCoO_3$ is metallic and ferromagnetic (F) with a near-300 K Curie temperature (T_C),[21] low V_O formation enthalpy (ΔH_{V_O}), and high V_O diffusivity (D_{V_O}), even under ambient conditions.[22,23] This

Received: July 22, 2021
Accepted: October 7, 2021
Published: October 25, 2021

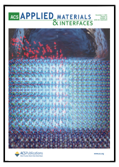

© 2021 American Chemical Society

https://doi.org/10.1021/acsami.1c13828
ACS Appl. Mater. Interfaces 2021, 13, 51205−51217

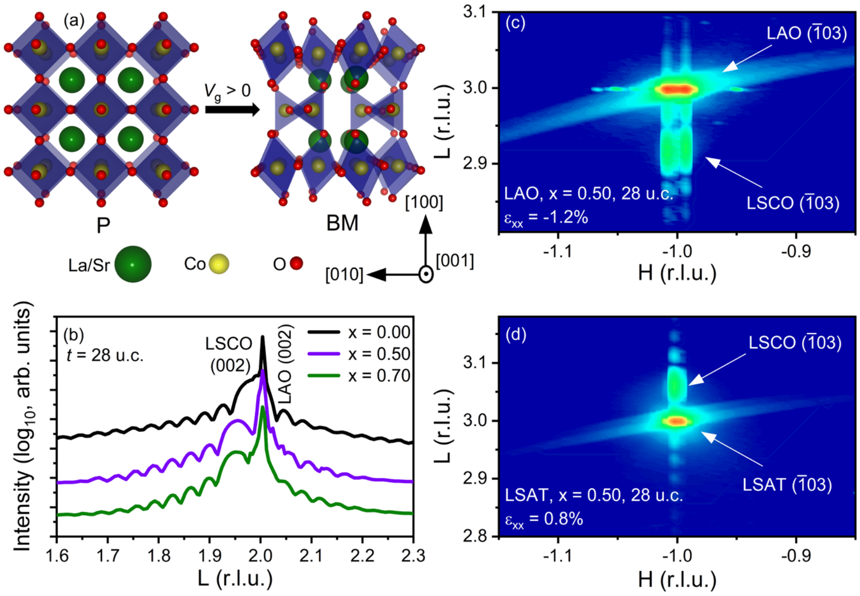

Figure 1. (a) Schematic crystal structures of perovskite (P, left) and BM (right) $La_{1-x}Sr_xCoO_{3-\delta}$ (LSCO). La/Sr (green), Co (yellow), and O (red) ions are shown, along with pseudocubic axes. (b) Specular SXRD scans around perovskite 0 0 2 reflections of 28-unit-cell-thick LSCO films on LAO(001) substrates for representative x of 0, 0.50, and 0.70 (offset for clarity). SXRD reciprocal space maps around the asymmetric $\bar{1}$ 0 3 reflections of representative $x = 0.50$ films on (c) LAO(001) and (d) LSAT(001). The magnitudes of the reciprocal lattice vectors H, K, and L (K = 0 here) are in substrate r.l.u. The "in-plane" strain values, ε_{xx}, are shown. The "double peak" structure in (c) is simply due to the typical twinning of LAO substrates.

material is thus highly susceptible to reduction, especially in thin-film form, V_O forming and proliferating readily. The beauty of this system, however, lies in the existence of V_O-*ordered* phases at specific oxygen deficiency δ, such as orthorhombic brownmillerite (BM) $SrCoO_{2.5}$ (*i.e.*, $Sr_2Co_2O_5$).[1,11−20] This forms by ordering V_O in lines along [101] directions, in alternate (100) planes, quadrupling the c-axis lattice parameter, and creating both octahedral and tetrahedral Co sites (Figure 1a).[1,11−20,24,25] The resultant phase has a very different electronic structure to P LSCO, exhibiting a clear energy gap, and insulating antiferromagnetism with a Néel temperature of 570 K.[1,11−20,26,27] The electronic, magnetic, and optical properties of the $SrCoO_{3-\delta}$ system can thus be massively modulated *via* topotactic transformation between P and BM and between an F metal and an antiferromagnetic (AF) insulator.[1,11−20]

Building on demonstrations of *thermal* cycling between the SCO P and BM,[15,20] and related phenomena *via* gettering with a reactive overlayer,[28,29] reversible *voltage*-driven BM ↔ P transformations have recently been established in several studies.[1,11−14,16−19] These employed electrolytes such as ZrO_2:Y_2O_3,[13,19] $NaTaO_3$,[14] and ionic liquids,[11,12,16−18] gating the as-deposited BM SCO to the P phase and back, verified by *operando* X-ray diffraction (XRD),[11,13,19] various spectroscopies,[11,12,16−19] and *operando* transmission electron microscopy (TEM).[17] This gating is nonvolatile, enabling *ex situ* measurements of magnetic properties,[11,14,16−20] electronic transport,[11,14,16,17,20] thermal transport,[12,20] and optical properties,[11] establishing extraordinary modulations in SCO, such as almost 5 orders of magnitude in room-temperature resistivity and approximately 220 K and 2 μ_B/Co in T_C and saturation magnetization.[11] Such findings naturally suggest potential applications, in magnetoionics, neuromorphic and stochastic computing, tunable photonics, and so forth.[1,7−9] Key attributes for such applications include wide property modulations, nonvolatility, and low power consumption (V_g is accompanied by little gate current), although reversibility and endurance over many cycles remain to be addressed.

While SCO is thus attractive for electrochemical gating, the stability of P SCO films under ambient conditions and mildly elevated temperatures is an issue.[11,15] Related to this, V_g-based P ↔ BM toggling has thus far been carried out exclusively from an as-deposited BM phase,[11−20] due to the difficulty of stabilizing P SCO in thin-film deposition. The latter has in fact required extreme oxidizing environments/treatments.[15] Exploration of related compositions for electrochemical gating has also been modest, although recent work highlights potential benefits. $SrCo_{1-x}Fe_xO_{3-\delta}$ was recently explored, for example, enabling BM ↔ P cycling with a P phase with room temperature ferromagnetism.[18] In this spirit, given the extensive prior work on the $La_{1-x}Sr_xCoO_{3-\delta}$ (LSCO) system,[30−32] it is remarkable that these compounds have not been studied for V_g-driven P ↔ BM transformations. This is particularly so given the extensive research on electrolyte gating of LSCO. At x = 0.5, for example, our recent work elucidated electrostatic *versus* electrochemical response in electrolyte-gated LSCO, highlighting the asymmetry of the V_g response.[22,33,34] Specifically, pristine (low δ) P films subject to *negative* V_g in ion-gel-based electrolyte-gate transistors were shown, at least at low V_g, to respond predominantly electrostatically through hole accumulation.[22,33,34] In essence, the low concentration of (thermodynamically stable) V_O in such systems favors hole doping over V_O annihilation during gating, thus increasing the average Co valence ($\bar{V}_{Co}$) from the initial 3.5+ (mixed Co^{3+}/Co^{4+}). This electrostatic effect persists to large negative V_g in ionic liquid/gel gating (approximately −3 to −4 V), at which point $\bar{V}_{Co}$ increases to the stage that LSCO becomes unstable toward V_O formation (an electrochemical response), leading to nonvolatility after V_g removal.[22,33,34] On the other hand, subjecting pristine (low δ)

P films to *positive* V_g leads to a dominant electrochemical effect *via* V_O formation,[22,33] assisted by the low ΔH_{V_O} and high D_{V_O}. This was established *via* nonvolatile transport response,[33] sensitivity to O_2,[33] and most directly, *operando* synchrotron XRD (SXRD),[22] X-ray absorption spectroscopy/X-ray magnetic circular dichroism (XAS/XMCD),[35] and polarized neutron reflectometry (PNR).[22] Such techniques detected the chemical expansion effect (*i.e.*, a cell volume increase) due to V_O formation[22] and the expected $\overline{V}_{Co}$ decrease,[35] PNR depth profiling revealing facile proliferation of V_O over tens of nanometer depths,[22] enabled by the outstanding D_{V_O} in LSCO.[22,23] These predominantly electrostatic (electrochemical) gate effects at negative (positive) V_g were subsequently utilized for voltage control of magnetism, spanning T_C modulations of approximately 150[34] and 190 K,[22] respectively.

The abovementioned progress with electrolyte gating of LSCO did not explore the largest positive V_g however, particularly at ambient temperatures.[22] It is thus unknown if the V_g-induced P → BM transformation established in SCO can be realized in LSCO and if so, over what x range. The influence of heteroepitaxial strain (which in SCO electrochemical gating can influence transformation dynamics[11]) is similarly unknown, as is the extent of modulation of electronic, magnetic, and optical properties across the putative P → BM LSCO topotactic transformation. The relative stability at lower x could also potentially enable gating from an as-deposited P phase (as opposed to the as-deposited BM in SCO[11−20]), establishing a straightforward new approach. Finally, a particularly intriguing finding in SCO electrochemical gating was the detection of hydrogen-intercalated compounds that can also be accessed by V_g tuning, in addition to the P and BM states.[11,36] Probing for the existence of such phases in LSCO would thus be of interest, as would any related x dependence.

In the abovementioned context, we provide here the first study of V_g-induced P → BM topotactic phase transformations as a function of x in LSCO, spanning almost the entire phase diagram ($0 \leq x \leq 0.70$). Ion-gel-gated epitaxial LSCO films are found to exhibit the P → BM transformation at essentially all x, including, crucially, $x \leq 0.50$ where the P phase is highly air-stable (Supporting Information, Figure S1). The threshold voltage for the P → BM transformation (V_{th}) is found to decrease substantially from approximately +2.7 V at $x = 0$ to negligible at $x = 0.70$, with epitaxial strain (which we study on three substrates) further decreasing V_{th}, particularly at low x. Potentially attractive for applications, V_{th} in LSCO is thus *tunable*, *via* both doping and strain. We thereby demonstrate voltage-controlled magnetic, electronic, and optical properties at $x = 0.50$, spanning ~220 K in T_C and at least 10^5 in resistivity, establishing competitive property modulations with SCO, but from a highly stable P starting point. $\overline{V}_{Co}$ is thus estimated as a function of V_g, and the results are interpreted in terms of key trends in ΔH_{V_O} and D_{V_O} with x and strain. The doping dependence, in particular, is connected to x-dependent trends in thermodynamic, rather than kinetic, factors (related to instability of the formal 4+ Co valence state in perovskites), connecting with recent theory. These findings thus substantially advance the understanding of the V_g-driven topotactic P → BM transformation in cobaltites, with both fundamental and technological implications.

2. EXPERIMENTAL METHODS

LSCO films ($0 \leq x \leq 0.70$) were deposited by high-pressure-oxygen sputtering from polycrystalline LSCO targets with the corresponding x, under previously optimized conditions.[22,33,34,37−39] $SrLaAlO_4$(001) (SLAO, space group $I4/mmm$, $a = b = 3.754$ Å and $c = 12.630$ Å), $LaAlO_3$(001) (LAO, space group $R\bar{3}c$, $a = b = 5.365$ Å and $c = 13.111$ Å, pseudocubic lattice parameter = 3.789 Å) and $(LaAlO_3)_{0.3}(Sr_2TaAlO_6)_{0.7}$(001) (LSAT, space group $Pm\bar{3}m$, $a = b = c = 3.868$ Å) substrates were employed. Substrates were first annealed at 900 °C in 1 Torr of flowing ultrahigh-purity (99.998%) O_2 for 15 min prior to deposition. Deposition was then performed at 600 °C substrate temperature (except for $x = 0$ films, for which 700 °C was used[39]), 60−70 W DC power, and 1.5 Torr O_2 pressure (resulting in 10−20 Å/min deposition rates), before cooling to ambient temperature in 600 Torr of O_2 at ~15 °C/min. Unless otherwise indicated, films in this study were 28 unit cells (u.c.)-thick (~11 nm), as determined from SXRD Laue fringes. Detailed structural characterization has been reported in prior work, encompassing high-resolution wide-angle XRD, SXRD, X-ray rocking curve analysis, X-ray reciprocal space mapping, grazing incidence in-plane XRD, grazing-incidence X-ray reflectivity, atomic force microscopy, cross-sectional scanning TEM with electron energy loss spectroscopy, and so forth.[22,33,34,37−41] Briefly, the films are phase-pure, epitaxial [(001)-oriented], and fully strained to these substrates (pseudomorphic) and have unit-cell-level surface roughness.[22,33,34,37−41]

Electrolyte-gate transistors were fabricated using previously reported methods.[22,33,34,42,43] Ar-ion milling and steel masks were first used to define 1.0 × 1.0 mm^2 (for electronic transport) or 3.5 × 4.0 mm^2 (for *operando* SXRD) LSCO channels on 5.0 × 5.0 or 10.0 × 10.0 mm^2 substrates, respectively. Gate and channel contacts [Mg (5 nm)/Pt (50 nm)] were then sputtered through another steel mask and rapid-thermal-annealed at 450 °C in flowing O_2. A schematic for the *operando* SXRD devices is shown in Figure 3a, highlighting the side-gate geometry. This was chosen as ideal for *operando* SXRD (to avoid X-ray beam blocking by a top gate),[22,42] although the response time is greatly increased (*i.e.*, the response is slower) compared to top-gate devices (due to the larger channel-gate separation with side gates).[22,33,42,43] "Cut and stick" ion gel electrolytes[44] were prepared by spin coating a 1:4:7 (by weight) solution of polymer−ionic-liquid−solvent on glass wafers to ~50 μm thickness. Poly(vinylidene fluoride-cohexafluoropropylene) was used as the polymer, 1-ethyl-3-methylimidazolium bis(trifluoro-methylsulfonyl)imide ([EMI][TFSI]) was used as the ionic liquid, and acetone was used as the solvent, and the gels were vacuum-annealed (70 °C, ~12 h) to remove any residual solvent. Sections of ion gel films were then cut from the glass wafers with a blade and laminated across the gate electrodes and LSCO channel to complete devices (see Figure 3a).[22,33,34,42,43]

Four-terminal DC transport measurements of ion-gel-gate LSCO transistors were performed in a Quantum Design Inc. Physical Property Measurement System and a closed-cycle He refrigerator. Keithley 2400 source-measure units were used for channel resistance measurements and to apply V_g. Reported in this work are both V_g-dependent measurements at 260 K (above the ~220 K freezing temperature of [EMI][TFSI]) and temperature (T)-dependent resistivity measurements after gating at 260 K for 30 min. The latter are complemented by *ex situ* measurements of magnetization *versus* T (5−300 K, in 100 Oe in-plane magnetic field) on 2.0 × 1.8 mm^2 channels in a Quantum Design Inc. Magnetic Property Measurement System. Room-temperature optical transmittance measurements were also performed *ex situ*, using a Cary 7000 ultraviolet/visible/near-infrared (UV/vis/NIR) spectrophotometer. Samples were mounted on an opaque holder with a 1 mm-diameter circular opening at the center to ensure illumination of only the LSCO channel (3.5 × 4.0 mm^2). Spectra were collected at normal incidence using an unpolarized light source and were referenced to the transmittance of air. *Operando* SXRD was carried out at beamline 12-ID-D of the Advanced Photon Source, using a six-circle Huber goniometer and a Pilatus II 100 K area detector.[22] Incident X-rays at 20 keV were employed (~0.62 Å), the spot size on the LSCO channel was ~300 μm, and measurements were made at 150 K in a liquid-N_2-flow cryocooler after V_g application at 280 K for 30 min. A discussion of beam damage mitigation procedures was provided earlier.[22]

3. RESULTS AND DISCUSSION

3.1. Structural Characterization. Shown first in Figure 1b are specular SXRD scans [intensity *I vs* scattering wavevector *L* in substrate reciprocal lattice units (r.l.u.)] around the 0 0 2 film and substrate reflections of representative LAO/LSCO (28 u.c.) films with *x* of 0, 0.50, and 0.70. Well-defined P LSCO film 0 0 2 peaks are evident, along with prominent Laue oscillations consistent with low surface and interface roughness. The latter is in agreement with our prior work, including cross-sectional TEM imaging and analysis.[37−41] As expected in P LSCO, the *c*-axis lattice parameter increases with *x*;[30−32,45] more detailed discussions of the *x*-dependent lattice parameters and other properties are provided below. Figure 1c,d then shows SXRD reciprocal space maps around the P $\bar{1}$ 0 3 reflections of $x = 0.50$ films on LAO (c) and LSAT (d), corresponding to illustrative "in-plane" strains ε_{xx} of −1.2% (compression) and +0.8% (tension), respectively. These 28 u.c. (~11 nm) films are indeed fully strained to the substrates (based on the identical *H* for the film and substrate peaks), with prominent Laue oscillations. Note that due to the *x*-dependent LSCO lattice parameter (Figure 1b), ε_{xx} varies with *x*, for $0 \leq x \leq 0.70$ spanning −2.1 to −1.4% on SLAO (large compressive strain), −1.2 to −0.6% on LAO (small compressive strain), and +0.8 to +1.5% on LSAT (tensile strain).

3.2. Transport and SXRD Characterization of the P → BM Transformation: Doping Dependence. Basic transport characterization of ion-gel-gated P LSCO films with *x* of 0, 0.10, 0.28, 0.50, and 0.70 is shown in Figure 2. We initially focus on films on LAO, that is, small compressive strains (−1.2 to −0.6%), studying the *x* dependence. Figure 2a,b (for $x = 0.50$) first illustrates the measurement scheme,[33,42] where various V_g values are applied for 30 min at 260 K in vacuum ($<10^{-5}$ Torr) (Figure 2a), and then the time (*t*) evolution of the gate-induced resistance change (ΔR) is tracked (Figure 2b). In the example shown in Figure 2b, $V_g = -3.0$ V (solid lines) is seen to induce ΔR that saturates at around −8%, the slow response, as already noted, being related to the side gate.[22,33,42,43] As discussed in Section 1, applying such negative V_g to pristine P LSCO ($x = 0.50$) films with low δ results in a predominantly electrostatic gate effect,[22,33,34] that is, an increase in hole doping and $\overline{V}_{Co}$. At some point, the induced elevated $\overline{V}_{Co}$ leaves the system unstable toward V_O formation, however, increasing δ. After removal of the negative V_g ($t > 30$ min in Figure 2a,b), substantial positive ΔR is then observed, that is, film resistance larger than at $t = 0$.[22,33,34] In contrast, but again consistent with Section 1, application of a positive V_g of +1.5 V to a pristine P LSCO ($x = 0.50$) film is seen (Figure 2a,b) to induce a positive ΔR (~6%) that is essentially entirely nonvolatile after V_g removal. This is due to predominantly electrochemical response at positive V_g through V_O formation (increased δ), as proven previously by *operando* SXRD,[22] XAS/XMCD,[35] and PNR[22] and reinforced below by SXRD observations of a cell volume increase and eventual P → BM transformation.

To track the full V_g dependence of the behavior in Figure 2b, two parameters are defined: $(\Delta R)_{gate}$, the gate-induced resistance change after 30 min, and $(\Delta R)_{nv}$, the resistance difference between $t = 0$ and the end of the cycle (60 min). In essence, $(\Delta R)_{gate}$ quantifies the gate effect, while $(\Delta R)_{nv}$ quantifies the nonvolatile resistance change. Figure 2c,d shows the V_g dependence of these quantities for $x = 0$, 0.10, 0.28, 0.50, and 0.70 LAO/LSCO films. Importantly, these were collected in a mode where one device was used for progressively larger negative V_g, followed by a second (nominally identical) device for progressively larger positive V_g. The situation on applying *negative* V_g from a pristine state is relatively straightforward for $x \leq 0.50$. Small, negative $(\Delta R)_{gate}$ occurs, consistent with the electrostatic hole accumulation just described.[22,33,34] Correspondingly, $(\Delta R)_{nv}$ is very small at all negative V_g for $x = 0$ and 0.10, increasing only modestly at $x = 0.28$. Again, such a positive $(\Delta R)_{nv}$ at the largest magnitudes of negative V_g arises from the induced increase in $\overline{V}_{Co}$, which leaves LSCO films unstable toward V_O formation after bias removal, thus inducing positive $(\Delta R)_{nv}$. As reported previously, by $x = 0.50$, this effect is prominent,[22,33,34] large positive $(\Delta R)_{nv}$ occurring at $V_g \leq -2.0$ V. Such effects are then dramatically enhanced at $x = 0.70$, the negative $(\Delta R)_{gate}$ becoming larger in magnitude (up to −65% at −4.0 V), accompanied by nonmonotonic $(\Delta R)_{nv}(V_g)$. This is ascribed to an abrupt increase in initial (as-deposited) δ in P LSCO films at $x > 0.50$, as discussed below.

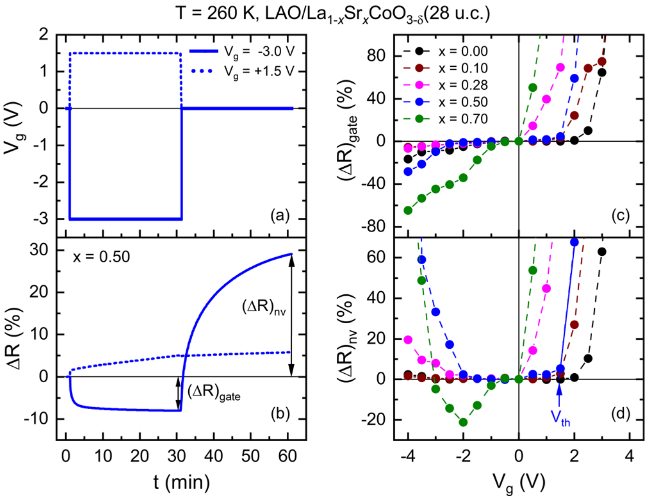

Figure 2. Time (*t*) evolution of (a) the gate voltage (V_g) and (b) the induced resistance change (ΔR) during voltage applications of +1.5 V (dashed lines) and −3.0 V (solid lines) to representative 28-unit-cell-thick $x = 0.50$ perovskite $La_{1-x}Sr_xCoO_{3-\delta}$ films on LAO. V_g dependence of (c) the gate-induced resistance change [ΔR_{gate}, defined in panel (b)] and (d) the nonvolatile resistance change [ΔR_{nv}, also defined in panel (b)] for 28-unit-cell-thick perovskite $La_{1-x}Sr_xCoO_{3-\delta}$ films ($x = 0$, 0.10, 0.28, 0.50, and 0.70) on LAO. All data were taken at 260 K in vacuum ($<10^{-5}$ Torr). As discussed in the text, positive and negative V_g data were collected on two different devices. The dashed lines in (c,d) simply connect points. The threshold voltage (V_{th}) is defined *via* linear extrapolation in (d), using $x = 0.50$ as an example.

The situation on applying *positive* V_g from a pristine state is relatively simpler. At low *x*, both $(\Delta R)_{gate}$ (Figure 2c) and $(\Delta R)_{nv}$ (Figure 2d) are first flat with increasing V_g before undergoing a rapid increase at fairly well-defined thresholds. This indicates a large (extending beyond the scale in Figure 2) and essentially entirely nonvolatile resistance change (compare Figure 2c,d) at some critical voltage, which is confirmed below to be coincident with a P → BM transformation in SXRD. We

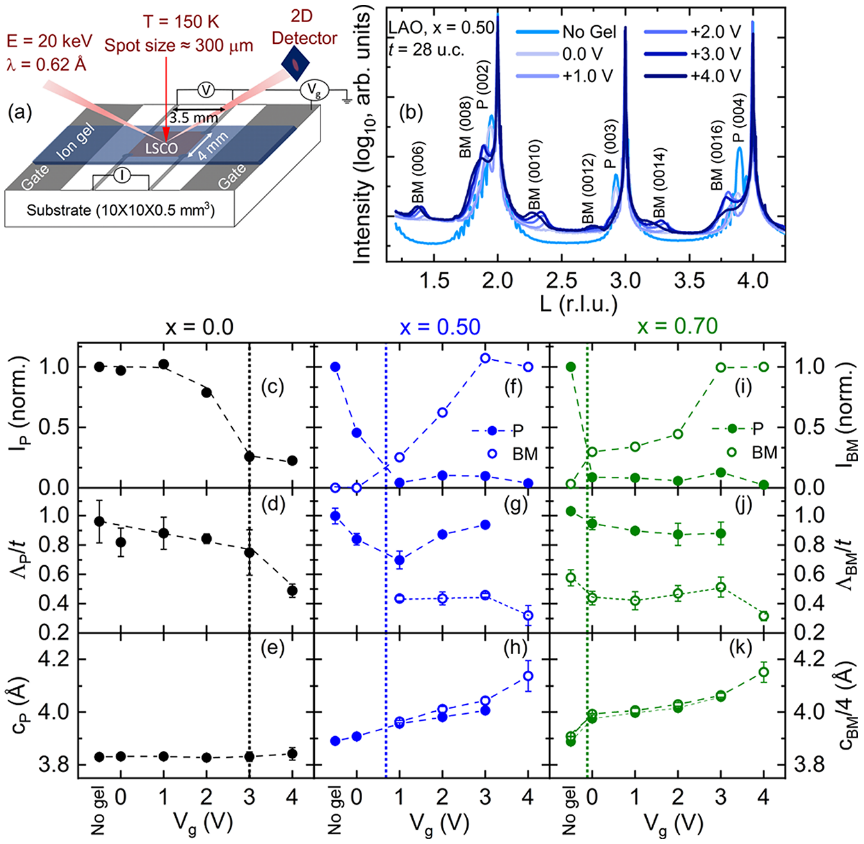

Figure 3. (a) Device schematic for *operando* SXRD on ion-gel-gated $La_{1-x}Sr_xCoO_{3-\delta}$ films. I, V, and V_g are the measurement current, measurement voltage, and gate voltage, respectively. (b) Representative wide-range specular *operando* SXRD scan of a 28-unit-cell-thick $x = 0.50$ $La_{1-x}Sr_xCoO_{3-\delta}$ film on LAO(001), ion-gel-gated at $V_g = 0.0$, +1.0, +2.0, +3.0, and +4.0 V. L is shown in substrate r.l.u. Perovskite (P) and BM reflections are labeled. (c−k) V_g dependence of the SXRD intensities of the P 0 0 2 and BM 0 0 6 peaks (I_P and I_{BM}, left and right axes, respectively, normalized to their maxima), average Scherrer lengths normalized to the as-grown film thickness for the P and BM phases (Λ_P/t and Λ_{BM}/t, left and right axes, respectively), and c-axis lattice parameters for the P and BM phases (c_P and $c_{BM}/4$, left and right axes, respectively). Data are shown for representative ion-gel-gated LAO/$La_{1-x}Sr_xCoO_{3-\delta}$ films with $x = 0$ (c−e), 0.50 (f−h), and 0.70 (i−k). Solid and open points are used for P and BM, respectively, and the "−0.5 V" points correspond to "no gel". The SXRD threshold voltage for the P to BM transformation (V_{th}) is marked by the vertical dotted lines. As discussed in the text, this is defined as the crossing point of I_P and I_{BM}; in (c−e), where no BM is directly detected, the dotted line is placed where I_P falls below 0.25. The dashed lines simply connect points. Scherrer lengths and lattice parameters are average values from all peaks, determined from Gaussian peak fitting; the error bars are one standard deviation. The (random) error bars in (c,f,i) are smaller than the points. Note that in (d,e,g,h,j,k), no points are plotted when the relevant P or BM intensity was too small to reliably fit peaks.

thus define a threshold voltage, V_{th}, by extrapolation of straight-line fits at high V_g (*e.g.*, the solid line for $x = 0.50$) to $\Delta R = 0$. Figure 2d illustrates this for $(\Delta R)_{nv}$, although a similar process for $(\Delta R)_{gate}$ results in similar V_{th}. The composition and strain dependence of this behavior will be discussed in detail below, the most significant observation for now being the striking reduction in V_{th} with x, which, in these low-compressive-strain LAO/LSCO films, falls from ~2.5 V at $x = 0$ to ~0 V at $x = 0.70$. V_{th} is thus *tunable*, the P → BM transformation at $x = 0.70$ becoming almost spontaneous.

The remainder of this paper focuses on positive V_g, seeking detailed understanding of the composition and strain dependence of the V_g-induced P → BM transformation and its impact on transport and magnetism. Figure 3 shows *operando* SXRD characterization of this transformation, starting with a schematic in Figure 3a. Figure 3b then shows a representative [LAO/LSCO ($x = 0.50$, 28 u.c.)] V_g dependence of specular SXRD data, that is, intensity *versus* L scans (see Supporting Information, Figure S2 for additional data at $x = 0$, 0.70). Prior to ion gel application ("no gel" in Figure 3b), such wide-range specular SXRD reveals high-intensity 0 0 2, 0 0 3, and 0 0 4 P peaks, accompanied by extensive Laue oscillations. After applying the ion gel, but before applying V_g ("0.0 V" in Figure 3b), changes in the SXRD are already detectable. First, the background intensity increases, presumably due to diffuse scattering from the ion gel. More significantly, the P peaks decrease in intensity and downshift in L, indicating a slight increase in c-axis lattice parameter. Increasing V_g to +1.0, +2.0, +3.0, and +4.0 V then induces dramatic changes, the 0 0 2, 0 0 3, and 0 0 4 P peaks being strongly suppressed, concomitant with the appearance of 0 0 6, 0 0 8, ..., 0 0 16 BM peaks. Such data conclusively demonstrate a P → BM transition, which we now analyze in detail.

Shown in Figure 3c−k are parameters extracted from SXRD of the type shown in Figure 3b, on films with $x = 0$ (left panels), 0.50 (middle panels), and 0.70 (right panels). The plotted quantities are the peak intensities (normalized to their maxima) of the P 0 0 2 and BM 0 0 6 peaks (I_P and I_{BM}, top panels, left and right axes, respectively), the average Scherrer lengths (Λ) extracted from P and BM peaks (normalized to the film thickness, t), and the c-axis lattice parameters of the P and BM phases (c_P and $c_{BM}/4$, respectively, on the left and right axes). As already noted, we focus on $V_g > 0$ only, *the points at "−0.5 V" signifying the "no gel" case*. Starting with the middle panels, that is, (f−h), the x = 0.50 composition shown in Figure 3b,f indicates undetectable BM intensity in the "no gel" and "0 V" cases. I_P and Λ_P/t (Figure 3f,g) nevertheless decrease upon gel application (from the Λ_P/t = 1.0 expected in a pseudomorphic epitaxial film), while c_P displays a corresponding small increase (Figure 3h). The situation then changes dramatically at +1.0 V, where I_P is strongly suppressed and I_{BM} turns on. Further increasing V_g leads to steady growth of I_{BM}, gradual increases in c_P and c_{BM}, and eventual flattening of I_{BM} at V_g > +3.0 V, where I_P becomes non-zero. Notably, Λ_{BM}/t is much smaller than Λ_P/t (this is clearly visible in the peak widths in Figure 3b), and the Laue oscillations in the P phase are absent in the BM phase.

Based on Figure 3b,f−h, we deduce a detailed picture of the V_g-induced P → BM transformation for x = 0.50. First, application of the ion gel apparently already results in slight reduction, as evidenced by the c_P increase between "−0.5" (no gel) and 0.0 V in Figure 3h. As discussed in Section 1, this is the chemical expansion effect due to V_O formation in P LSCO,[22] the fact that this occurs at V_g = 0 being consistent with prior work;[33] in ionic liquid/gel gating, typically either the ionic liquid cation or anion has an affinity for the surface of the gated material, leading to a gate effect even at V_g = 0.[33,42] As evidenced by the accompanying decrease in both I_P and Λ_P/t (Figure 3g,h), this reduction of the P phase apparently deteriorates crystalline coherence. There is no detectable BM at V_g = 0 after gel application, however, indicating only an increase in δ in the P phase.

At $V_g \geq$ +1.0 V, the situation is very different. The first thing to note is the distinctly gradual evolution in lattice parameters with V_g (Figure 3h), related to the continuous progression from the P 0 0 2 peak at V_g = 0 to the BM 0 0 8 peak at V_g = +4.0 V (Figure 3b). This indicates a gradual, not discontinuous, increase in δ with V_g. Interestingly, the literature on voltage-triggered BM ↔ P transitions in related $SrCoO_{3-\delta}$ suggests no consensus on this point, the nature of the transition being variable and often different for BM → P than P → BM.[11−20] By +1.0 V, I_P is dramatically suppressed (Figure 3f) and I_{BM} becomes nonzero (consider Figure 3f and the 0 0 6 BM peak in Figure 3b), indicating that not only has δ increased, but ordering of V_O into the BM motif has occurred. At this point, both P and BM phases are detectable, which remains true up to +3.0 V (Figure 3f). It is only at V_g > +3.0 V that I_{BM} saturates and I_P vanishes, indicating phase-pure BM. It is also only at +3.0 V that the ratio of BM 0 0 8 to 0 0 6 intensities becomes comparable to the literature for phase-pure BM;[11−20] below this V_g, the BM 0 0 8 to 0 0 6 ratio is far above expectations (see Supporting Information, Figure S3), indicating that the intensity in the BM 0 0 8/P 0 0 2 region derives from downshifted P 0 0 2 intensity due to increasing δ. Together, Figure 3b,f−h thus reveals an evolution from phase-pure P at V_g < +1.0 V (with increasing δ but disordered V_O) to a regime of P−BM phase coexistence (both V_O-disordered and V_O-ordered regions) to phase-pure BM at V_g > +3.0 V (entirely V_O-ordered). While this is not commented on in the gated SCO literature, our observations, particularly the distinct phase coexistence regime, are consistent with a first-order transformation.[46] In our side-gate geometry (Figure 3a), the P−BM phase boundary would then be expected to migrate laterally across the gated LSCO film[17] in the +1.0 V ≤ V_g ≤ +3.0 V window. To facilitate simple and approximate comparison to V_{th} from transport, we nevertheless simply define a single SXRD P → BM threshold voltage as the linearly interpolated point at which I_P and I_{BM} cross, for example, 0.7 V for x = 0.50 in Figure 3f, as marked by the vertical dotted line.

As final comments on the P → BM transformation in these LAO/LSCO (x = 0.50) films, we first note that the distinctly lower Λ_{BM}/t than Λ_P/t indicates lesser through-plane structural coherence, likely indicating multiple BM domains through the film thickness, potentially with additional microstrain contributions, that is, a distribution in local lattice parameters. Related to this, the BM reflections in Figure 3b have no Laue fringes, indicating substantial disorder associated with these BM domains. Future work to understand how this structural disorder in the BM influences the microstructure after gating back to the P phase at negative V_g would clearly be worthwhile, with important potential implications for reversibility and endurance. Second, we note that our data at x = 0.50 exclusively evidence BM-like V_O-ordered phases at high V_g, with the quadrupled lattice parameter with respect to the P phase; we find no evidence, for example, of Grenier phases with alternative V_O modulations at this x. Third, as noted in Section 1, in SCO, ordered *H*-intercalated phases have been detected in addition to P and BM, *via* a second transformation with further expansion of the lattice parameter. Our data on LSCO (*e.g.*, Figure 3b,e,h,k) provide no obvious indications of such phases, however. As discussed below, we also do not observe any of the magnetic or optical characteristics of these ordered *H*-intercalated phases (*i.e.*, weak F behavior and very wide gaps). These observations could indicate suppression of such protonation effects with La incorporation in SCO or simply disordered *H* incorporation. Future work with techniques such as secondary ion mass spectrometry and neutron reflectivity could shed light on this.

Turning to x other than 0.50, as shown in Figure 3i−k, the main difference in behavior for x = 0.70 is that, consistent with transport (Figure 2c,d), BM phase formation is essentially spontaneous at V_g = 0 after gel application (Figure 3i). With further increase in V_g, the situation is then similar to x = 0.50: I_{BM} gradually increases and saturates, I_P eventually becomes undetectable (Figure 3i), Λ_{BM}/t is substantially reduced relative to Λ_P/t (Figure 3j), and c_P and c_{BM} gradually increase (Figure 3k). Also consistent with Figure 2c,d, the situation at x = 0 is very different. Figure 3c−e in fact reveals only P peaks, with no detectable BM at any V_g. Nevertheless, a clear change occurs around +3.0 V, where I_P dramatically drops (Figure 3c), Λ_P/t falls (Figure 3d), and a small increase in c_P is detected (Figure 3e). We hypothesize that while the long-range V_O order required for BM reflections is not yet present here, it is possible that short-range V_O order occurs, as is well known even in as-deposited LSCO films at higher x.[25,37,38,40,41] This phenomenon could also occur as a precursor to the onset of BM reflections at higher x, perhaps associated with the decrease in I_P prior to BM detection in Figure 3f, for example. Moreover, as shown in Supporting Information Figure S2 (top panel), we find evidence of a broad hump in intensity to the left of the P 002, 003, and 004 peaks after gating to the highest voltages. This could potentially indicate some formation of a Grenier phase at x = 0 (*i.e.*, a different V_O order modulation period to BM), which would be worthy of further investigation in future work.

The central issue of the x dependence of the threshold voltage for the P → BM transformation is highlighted in Figure 4, which plots V_{th} from both transport (*e.g.*, Figure 2c,d) and SXRD (*e.g.*, Figure 3c−k). The black circles in Figure 4 are for LAO/LSCO; the solid circles correspond to transport [an

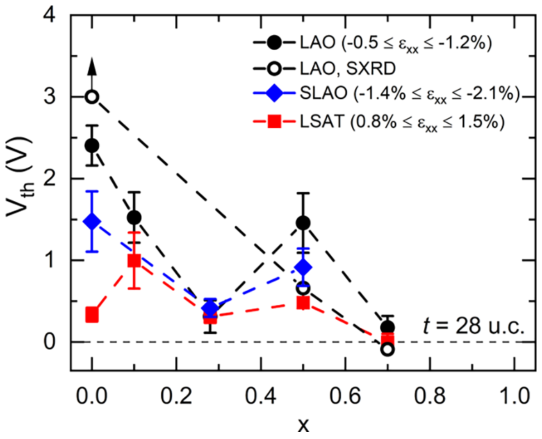

Figure 4. Threshold voltage for the perovskite (P) to BM transformation (V_{th}) *vs* x for ion-gel-gated 28-unit-cell-thick $La_{1-x}Sr_xCoO_{3-\delta}$ films. V_{th} is shown from both transport (solid points, averaged from both Figure 2c,d) and *operando* SXRD (open points). Data are shown for films on LAO, SLAO, and LSAT substrates, labeled with the "in-plane" ε_{xx} range (due to the varied x). Error bars on the points from transport correspond to the fitting errors on the extrapolations to determine V_{th}, as illustrated by the solid line in Figure 2d. Error bars on the points from SXRD (which are smaller than the points themselves) correspond to analogous fitting errors on the interpolations used to determine the crossover points for the P and BM intensities (see, *e.g.*, Figure 5f).

average from $(\Delta R)_{gate}(V_g)$ (Figure 2c) and $(\Delta R)_{nv}(V_g)$ (Figure 2d)], and the open circles correspond to SXRD (dotted vertical lines in Figure 3c−k). Consistent with inspection of Figures 2c,d and 3c−k, an overall reduction in V_{th} with x is revealed in Figure 4 for LAO/LSCO, transport and SXRD being reasonably consistent, given the error bars, the estimation of which is discussed in the figure caption. V_{th} drops from at least 2.4 to 3.0 V at $x = 0$ (where the upward arrow indicates that long-range BM order was not detected in SXRD) to negligible at $x = 0.70$. Below, we discuss specific conclusions regarding the origin of the overall decrease in V_{th} with x and its apparent nonmonotonicity in Figure 4; for now, we note only that V_{th} is clearly doping-tunable, a feature that would appear attractive for applications such as neuromorphic computing.[1,7−9,47−49]

3.3. Transport and SXRD Characterization of the P → BM Transformation: Strain Dependence. Also shown in Figure 4 are data for LSCO films on SLAO (blue diamonds) and LSAT (red squares), as opposed to the LAO substrates emphasized thus far. As noted in the figure, ε_{xx} on SLAO is −2.1 to −1.4% (*i.e.*, stronger compression than LAO), whereas ε_{xx} on LSAT is +0.8 to +1.5% (*i.e.*, tensile strain), exposing another important conclusion. Specifically, both higher compressive strain (on SLAO) and tensile strain (on LSAT) result in lower V_{th}, particularly at low x, that is, where V_{th} in LAO/LSCO is large. The transport and SXRD data underpinning this are summarized in Figure 5. Shown first in Figure 5a are $(\Delta R)_{nv}$ *versus* V_g data at $x = 0$, on SLAO ($\varepsilon_{xx} = -2.1\%$), LAO ($\varepsilon_{xx} = -1.2\%$), and LSAT ($\varepsilon_{xx} = +0.8\%$) (see Supporting Information, Figure S4 for raw data, *i.e.*, the equivalents to Figure 2c,d on LSAT and SLAO). The trend with heteroepitaxial strain is clear, V_{th} being maximum at +2.4 V under small compressive strain (LAO), falling to +1.5 V under higher compressive strain (SLAO), and decreasing to only +0.3 V under tensile strain (LSAT). Larger ε_{xx} magnitudes thus decrease V_{th} at low x, tensile strain having the strongest influence. Representative wide-range specular *operando* SXRD as a function of V_g is shown in Figure 5b, this time using LSAT/LSCO (x = 0.50) as an example (see Supporting Information, Figure S5 for equivalent data on SLAO). The 0 0 2 P peak (now to the right of the substrate peak) is strongly suppressed with increasing V_g, while 0 0 L BM peaks emerge, again signaling a P → BM transformation. The systematics are analyzed in Figure 5c−k for $x = 0.50$ films on SLAO (left panels), LAO (middle panels), and LSAT (right panels), where the plotted quantities are identical to Figure 3. By now familiar behavior occurs in all three cases, particularly the decrease in I_P with V_g, the onset of I_{BM}, the smaller Λ_{BM}/t than Λ_P/t, and the gradual increase in c_P and c_{BM} with V_g. We thus again conclude an evolution from phase-pure epitaxial P to P−BM coexistence, to phase-pure BM. As in Figure 3, the vertical dotted lines indicate the linearly interpolated point where I_P and I_{BM} cross. This is approximately strain-independent at x = 0.50 (Figure 5c−k), although it can be seen from Figure 4 that V_{th} drops significantly with strain as $x \rightarrow 0$, particularly under tension. Specific conclusions regarding the origin of this decrease in V_{th} with increasing strain magnitudes will be presented later; for now, we note only that V_{th} is clearly strain-tunable, in addition to being composition-tunable, adding further flexibility for applications. As a final comment on Figure 5, note that on all substrates, the V_g-induced BM phase is 0 0 1 oriented, meaning that the alternating planes of the V_O order are parallel to the substrate/film interface. This is consistent with the BM phase being under compressive strain with respect to all three substrates.[25,40]

3.4. Control of Magnetic, Transport, and Optical Properties. Switching from characterization of the V_g-induced P → BM transformation to understanding the extent to which it can control magnetic, transport, and optical properties, Figure 6a,b shows *ex situ* T-dependent measurements of magnetization (M, in a 100 Oe in-plane field) and resistivity (ρ) after gating to various V_g. These are shown for the representative case of LSAT/LSCO [x = 0.50, 35 u.c. (∼13.5 nm)]. Such films are initially F and metallic, the in-plane magnetization, ∼220 K Curie temperature (Figure 6a), positive $d\rho/dT$ at all T, and ∼100 $\mu\Omega$ cm residual resistivity (Figure 6b) agreeing with prior reports on moderately tensile-strained x = 0.50 P LSCO films of comparable t.[37,38]

As expected based on Figures 3 and 5, application of ion gels while maintaining $V_g = 0$ already has some impact, ρ increasing slightly in response to increased δ. Increasing V_g to +1.0 and then +1.2 V induces more significant changes, T_C dropping by ∼14 K (Figure 6a), M falling noticeably (Figure 6a), and the apparent ρ increasing over 10-fold to a state with negative $d\rho/dT$ at all T (Figure 6b). It should be noted here that while the nominal $\rho(T)$ is plotted in Figure 6b, absolute values and the exact form of $\rho(T)$ at intermediate V_g should be treated with caution due to the expectation of both depthwise and lateral inhomogeneity. Depthwise variations in δ and the extent of V_O order are of course expected in such gated devices, lateral inhomogeneity likely being accentuated here by P−BM phase coexistence, and the side-gate geometry (Figure 3a). Above +1.2 V, more dramatic effects emerge, V_g of +1.4 V through +2.0 V completely suppressing the F magnetization and T_C. This occurs *via* a reduction in T_C to ∼170 K, followed rapidly at higher V_g by vanishing of F magnetization. We believe that this is consistent with the bulk LSCO phase diagram, where the magnetic ordering temperature rapidly decreases on

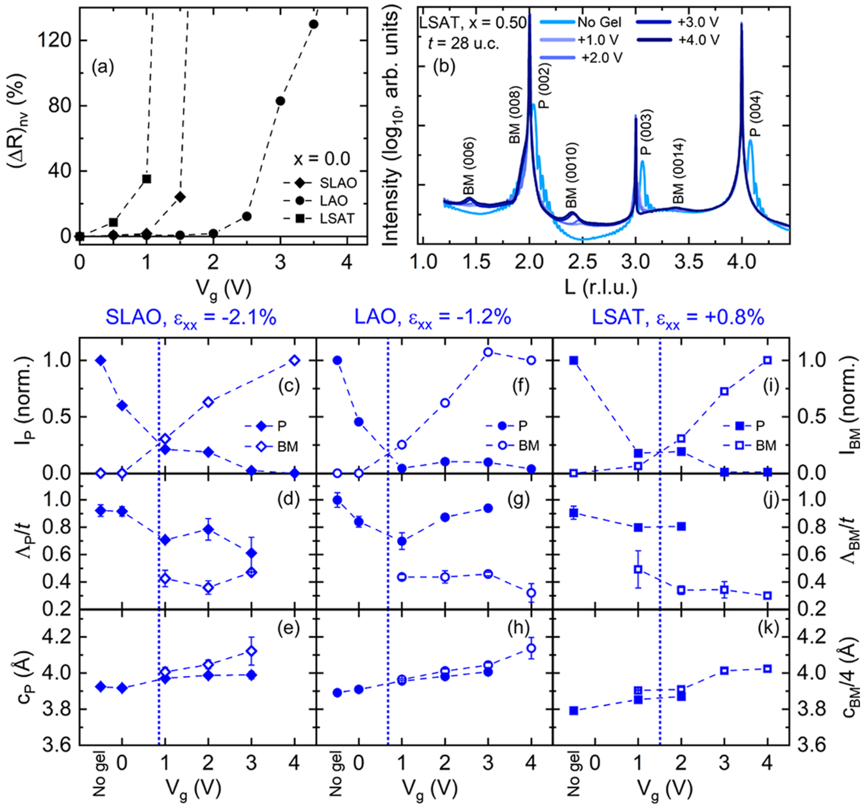

Figure 5. (a) Positive gate voltage (V_g) dependence of the nonvolatile resistance change (ΔR_{nv}) in ion-gel-gated 28-unit-cell-thick $LaCoO_{3-\delta}$ films ($x = 0$) on SLAO, LAO, and LSAT substrates. Conditions are the same as for Figure 2d. (b) Representative wide-range specular *operando* SXRD scan of a 28-unit-cell-thick $x = 0.50$ $La_{1-x}Sr_xCoO_{3-\delta}$ film on LSAT(001), ion-gel-gated at V_g = 0.0, +1.0, +2.0, +3.0, and +4.0 V. L is shown in substrate r.l.u. Perovskite (P) and BM reflections are labeled. (c−k) V_g dependence of the SXRD intensities of the P 0 0 2 and BM 0 0 6 peaks (I_P and I_{BM}, left and right axes, respectively, normalized to their maxima), average Scherrer lengths normalized to the as-grown film thickness for the P and BM phases (Λ_P/t and Λ_{BM}/t, left and right axes, respectively), and c-axis lattice parameters for the P and BM phases (c_P and $c_{BM}/4$, left and right axes, respectively). Data are shown for the representative ion-gel-gated $x = 0.50$ $La_{1-x}Sr_xCoO_{3-\delta}$ films on SLAO (c−e), LAO (f−h), and LSAT (i−k). Solid and open points are used for P and BM, respectively, and the "−0.5 V" points correspond to "no gel". The SXRD threshold voltage for the P to BM transformation (V_{th}) is marked by the vertical dotted lines; as discussed in the text, this is defined as the crossing point of I_P and I_{BM}. The dashed lines simply connect points. For the three substrates, the "in-plane" strains, ε_{xx}, are shown. Scherrer lengths and lattice parameters are average values from all peaks, determined from Gaussian peak fitting; the error bars are one standard deviation. The (random) error bars in (c,f,i) are smaller than the points. Note that in (d,e,g,h,j,k), no points are plotted when the relevant P or BM intensity was too small to reliably fit peaks.

lowering the doping below $x = 0.18$, as long-range F order breaks into a magnetically phase-separated cluster glass.[30−32] This transition is driven here *via* decreasing *effective* doping, $x_{eff} = x - 2\delta(V_g)$, that is, by each induced V_O compensating two doped holes (in the simplest model[34,41]), along with the simultaneous ordering of V_O that drives the topotactic transformation to non-F BM. (We note as an aside that no clear evidence of weak F previously found in H-intercalated SCO is apparent at high V_g, consistent with the absence of such phases in our SXRD). Commensurate with the observed changes in $M(T)$, ρ at V_g = +2.0 V increases to as much as ~0.1 Ω cm, that is, 10^3 times larger than the initial state. Beyond this, +3.5 V then results in ρ(300 K) ≈ 1 Ω cm, increasing rapidly to ~10 Ω cm at 250 K, below which DC transport measurements become prohibitively difficult.

In totality, ρ in this illustrative LSAT/LSCO ($x = 0.50$, 35 u.c.) case can thus be tuned over at least 5 orders of magnitude (much more at low T) *via* the ion-gel-gating-induced P → BM transformation, the accompanying T_C modulation being ~220 K, that is, from ~220 to 0 K. Importantly, these findings map well to the corresponding V_g-dependent LSAT/LSCO ($x = 0.50$) SXRD data (Figure 5i−k). Specifically, the clear P−BM phase coexistence between +1.0 and +3.0 V (Figure 5i), the crossing of P and BM intensities at ~1.5 V (where M becomes rapidly suppressed in Figure 6a), and the onset of phase-pure BM at ≥+3.0 V [where $\rho(T)$ becomes strongly insulating in Figure 6b] all point to consistency between SXRD and transport/magnetometry. An interesting goal for future work will be to probe any magnetic order in the V_g-induced LSCO BM state, which, while clearly non-F, is not entirely clarified by the current measurements. An x-dependent study of this issue in LSCO would clearly be worthwhile, perhaps *via* neutron diffraction. Even the heavily studied $x = 1$ (SCO) composition would benefit from such effort, as it appears that the suspected AF order in thin-film BM has not been rigorously verified.

As shown in Figure 6c, the V_g-driven P → BM transition in LSAT/LSCO [$x = 0.50$, 30 u.c. (~11.5 nm)] films also has a dramatic impact on optical (UV/vis/NIR) transmittance. The initial P state exhibits relatively weakly energy-dependent transmittance, but with a noticeable decrease at energies less than ~1.2 eV, consistent with the free carrier absorption expected of a metal. After gating at V_g = +3.0 V, the latter effect is eradicated. The transmittance in fact increases substantially relative to ungated LSCO, specifically below photon energies

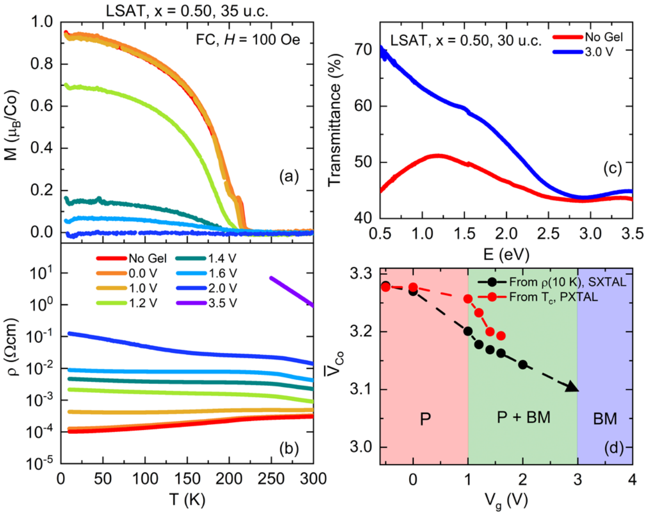

Figure 6. Temperature (T) dependence of (a) the in-plane magnetization (M) measured in 100 Oe after field cooling (FC) in 10,000 Oe and (b) the zero-field resistivity (ρ) of a 35-unit-cell-thick $x = 0.50$ $La_{1-x}Sr_xCoO_{3-\delta}$ film on LSAT ion-gel-gated to gate voltages V_g = 0.0, +1.0, +1.2, +1.4, +1.6, +2.0, and +3.5 V. (c) Energy-dependent optical (UV/vis/NIR) transmittance spectra for 30-unit-cell-thick $x = 0.50$ $La_{1-x}Sr_xCoO_{3-\delta}$ films on LSAT prior to ion gel application (red) and after V_g = +3.0 V (blue). Spectra were collected at room temperature, using unpolarized light at normal incidence, and are referenced to the transmittance of air. (d) V_g dependence of the average Co valence ($\bar{V}_{Co}$) estimated by comparison to both bulk single-crystal 10 K resistivities [ρ(10 K)] and bulk polycrystalline Curie temperatures (T_C), as discussed in the text. The colored shading indicates the phase-pure P, phase coexistence, and phase-pure BM regions, as deduced from SXRD (Figure 5i−k). As in Figures 3 and 5, "V_g = −0.5 V" corresponds to the "no gel applied" case.

of ~3 eV; by 0.5 eV, the two transmittances differ by as much as 70 *versus* 45%. Such observations are in good qualitative agreement with optical studies of the P → BM transformation in SCO, which report similar features in optical transmittance spectra[11] and a prominent decrease in the absorption coefficient of the BM phase below a direct band gap of 2−3 eV.[11,50,51] The transmittance spectra in Figure 6c thus provide yet further evidence, *via* optical spectroscopy, that our gate-induced BM LSCO has the anticipated electronic structure, specifically an insulating, gapped nature.

With regard to quantification, while not yet carried out to our knowledge in the literature on the V_g-driven BM ↔ P transformation in $SrCoO_3$, magnetic and transport data of the type in Figure 6a,b also enable estimates of the V_g-dependent δ and thus $\bar{V}_{Co}$. To do this, we assume that the electronic and magnetic behavior of these relatively thick gated films is controlled by $x_{eff} \approx x - 2\delta(V_g)$, the well-documented x-dependent bulk properties establishing baseline behavior for *relatively* negligible δ. We use two well-established bulk relations for this purpose: the low T (10 K) single-crystal ρ *versus* x[34] and the polycrystalline T_C *versus* x,[32,33] resulting in the black and red points in Figure 6d. Explicitly, plotted here is the mean Co valence, $\bar{V}_{Co}(V_g) \approx 3 + x_{eff}(V_g)$, where $x_{eff}(V_g)$ is estimated by comparing ρ(10 K) and T_C at each V_g to the established bulk (relatively V_O-free) $\rho(x)$ and $T_C(x)$. This procedure was previously validated even in ultrathin gated LSCO films.[33,34] The two methods are seen to be in reasonable agreement in Figure 6d (at least to V_g = +1.6 V, where the F state is suppressed and T_C can no longer be used), the significant finding being the approximately linear decrease in $\bar{V}_{Co}$ with V_g. Shaded on Figure 6d are the approximate pure P, P + BM, and pure BM regimes from SXRD (Figure 5i). While our $\bar{V}_{Co}$ estimates apply strictly only to the P phase, transport will be dominated by the P phase even in the P−BM

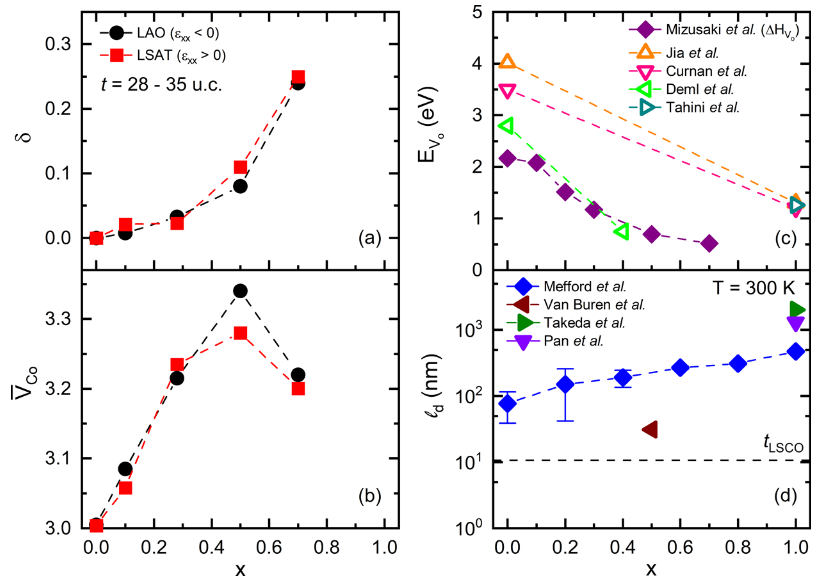

Figure 7. Sr doping (x) dependence of (a) oxygen deficiency (δ) estimated by comparison to bulk single-crystal 10 K resistivities and (b) estimated average Co valence ($\bar{V}_{Co}$) of as-deposited $La_{1-x}Sr_xCoO_{3-\delta}$ films (28−35 u.c. thick) on LAO and LSAT substrates. Literature values of the x-dependent (c) oxygen vacancy formation energy (E_{V_O}) and (d) 300 K oxygen vacancy diffusion length (l_D) for $La_{1-x}Sr_xCoO_{3-\delta}$. In (c), the values of Mizusaki *et al.*[53] are experimentally measured enthalpies from thermogravimetry, while the values of Jia *et al.*,[55] Curnan and Kitchin,[54] Deml *et al.*,[56] and Tahini *et al.*[57] are from DFT. In (d), the values of Mefford *et al.*,[59] Pan *et al.*,[60] Takeda *et al.*,[61] and Van Buren *et al.*[62] are from electrochemical chronoamperometry. The dashed line simply connects the data points of Mefford *et al.*[59] The horizontal dashed line marks the thickness of $La_{1-x}Sr_xCoO_{3-\delta}$ films (28 u.c.).

https://doi.org/10.1021/acsami.1c13828
ACS Appl. Mater. Interfaces 2021, 13, 51205−51217

coexistence region, justifying plotting such data beyond the phase-pure P region.

Notably, the "no gel" (*i.e.*, "−0.5 V") and $V_g = 0$ points in Figure 6d are at $\bar{V}_{Co} \approx 3.28$, not the nominal 3.50 for an $x = 0.50$ LSCO film. This is unsurprising, particularly for films under tension on LSAT, indicating non-negligible δ, as-deposited. To explore the x dependence of this, which could play a role in our finding of decreasing V_{th} with x (Figure 4), the method of comparison to the low T bulk single-crystal $\rho(x)$[34] was applied to pristine P films with x = 0, 0.10, 0.28, 0.50, and 0.70, resulting in the estimated $\delta(x)$ and $\bar{V}_{Co}(x)$ in Figure 7a,b. Under both tensile and compressive strain (LSAT and LAO), the as-grown δ is negligibly small at $x = 0$, as expected (this corresponds to relatively stable Co^{3+}), increasing only weakly to $x = 0.28$. Further increasing x then leads to not only rapidly increasing δ (reaching ∼0.25 at $x = 0.70$) but also distinct strain dependence, δ becoming larger under tension than compression. The effect on $\bar{V}_{Co}(x) \approx 3 + x - 2\delta(x)$ (Figure 7b) is dramatic, increases in Sr doping above $x = 0.50$ being outweighed by the increase in δ, leading to *lower* x_{eff} and $\bar{V}_{Co}$. This is similar to the behavior in bulk LSCO reported by Jonker and Van Santen[30] and reinforced in refs 31 and 32. This is typically ascribed to decreasing ΔH_{V_O} as $x \to 1$, due to the instability of formal 4+ Co valence in octahedral coordination, as in perovskites such as SCO. This is consistent with the aforementioned challenges with stability of $SrCoO_3$ films[11,13] and the fact that synthesis of bulk $SrCoO_3$ requires high O_2 pressure.[21] Clearly, this growing instability to V_O formation with increasing x and the increased initial δ at high x and under tensile strain are important as we consider the origin of the V_{th} trends uncovered in this work.

3.5. Interpretation of the Composition and Strain Dependence of the P → BM Transformation.

The decreasing V_{th} for the P → BM transformation with increasing x and strain magnitude (particularly under tension) are central results of this work, which we now attempt to understand. Clearly, the V_g-driven P → BM transformation in LSCO requires initial formation of V_O in the P LSCO near the LSCO/ion gel interface,[22,47,48,52] subsequent proliferation of these V_O's through the film thickness,[22,47,48] and ordering of these V_O's into the BM motif.[24,25,47,48] The initial δ in the P phase, ΔH_{V_O}, D_{V_O}, and the energetics/kinetics of the V_O disorder/order transition are thus all potentially important factors, which we now consider. As discussed in the prior section, the initial δ in the as-deposited P LSCO films clearly increases with x and strain (particularly tensile) (Figure 7a), meaning that the V_g-driven P → BM transformation is being induced from a state with δ closer to the nominal 0.5 in BM. As already noted, we ascribe this x dependence to decreasing ΔH_{V_O} with x. As shown in Figure 7c, both experimental reports of ΔH_{V_O}[53] and density functional theory (DFT) calculations of the formation energy (E_{V_O})[54−57] support substantial decreases with x in LSCO. Scatter between various studies exists, but the enthalpies/energies tend to decrease by a substantial ∼2 eV from $LaCoO_{3-\delta}$ to $SrCoO_{3-\delta}$. DFT studies as a function of heteroepitaxial strain are similarly revealing, suggesting decreased E_{V_O} with increasing strain magnitude (both compressive and tensile),[58] at least at $x = 0.50$. We thus conclude that these established trends impact our observed $V_{th}(x, \varepsilon_{xx})$ in at least two ways: by leading to increased initial δ at higher x and $|\varepsilon_{xx}|$ in P films grown (and cooled) under fixed conditions and by enabling more facile V_g-induced formation of V_O at the LSCO/ion gel interface at higher x and $|\varepsilon_{xx}|$. As pointed out by Zhang *et al.*,[47,48] these two points are connected, nonzero initial δ being capable of lowering the P → BM transformation barrier.

As gating proceeds, proliferation of V_O through the film is required, rendering D_{V_O} important.[1,11−20,22,28,29,33,34] Experimental data on this in P LSCO (from electrochemical chronoamperometry[59−62]) are shown in Figure 7d. As noted previously[22] and as is likely at the root of the extensive recent literature focus on electrochemical gating of cobaltites,[1,11−20,22,28,29,33,34] D_{V_O} in LSCO is exceptionally high,[23] to the degree that even at 300 K, the V_O diffusion length, $l_d = (D_{V_O}t)^{1/2}$, on the 30 min time scales here, is substantial. As illustrated by the blue points and the dashed vertical line in Figure 7d, the data of Mefford *et al.*,[59] for example, suggest several-hundred-nm V_O diffusion lengths under our gating conditions, significantly larger than the film thickness (28 u.c.), even at $x = 0$ ($LaCoO_3$). This indicates that at these V_g application rates, the reduction of P LSCO is not diffusion-limited, meaning that thermodynamic factors, not kinetics, control the x- and strain-dependent V_{th}. We offer two additional thoughts on this. First, this situation could clearly change for higher frequency gating in top-gated devices, and second, it is not yet understood what role V_g plays in assisting V_O diffusion; both of these issues are ripe for further study.

After initial V_O formation at the P LSCO/ion gel interface and subsequent depthwise V_O diffusion, the final issue is the V_O disorder/order transition that constitutes the P → BM transformation. Important in this context is the recent work of Zhang *et al.*,[47,48] focused on DFT- and model-based electronic structure understanding of the P → BM transformation specifically in LSCO. Key findings include reproduction of the P cell expansion with increasing δ, detailed understanding of the structure and electronic structure with δ (including the opening of a gap), confirmation of decreasing E_{V_O} with x, and, perhaps most significantly, calculations of V_{th} for the P → BM transformation.[47,48] The latter predict not only decreasing V_{th} with x but also absolute values in the 0.5−1.2 V range, in reasonable agreement with our data (Figure 4).[47,48] Moreover, the dependence of V_{th} on the initial δ is also predicted to be *nonmonotonic*,[47,48] providing a potential explanation for another noticeable feature of Figure 4, namely, the apparent dip in V_{th} around $x = 0.28$. According to Figure 7a, the initial δ at this x is significant, reaching ∼0.03. In terms of the overall decrease with x, approximate magnitude, and nonmonotonic behavior, we thus conclude at least qualitative agreement with literature trends in key thermodynamic and kinetic factors with doping and strain, approaching quantitative agreement with recent computational theory. Particularly, given the significant effect of strain on V_{th} even at $x = 0$ (see Figure 4), where the initial δ is small and negligibly strain-dependent, it would be of high interest to extend such DFT calculations to different heteroepitaxial strain states.

4. SUMMARY

We have presented the first study of the voltage-induced topotactic perovskite to BM transformation across almost the entire phase diagram of ion-gel-gated $La_{1-x}Sr_xCoO_{3-\delta}$ ($0 \le x \le 0.70$), employing epitaxial films on three different substrates to understand the impact of strain. Electronic transport and *operando* SXRD confirm that the perovskite to BM transformation can be driven at essentially all x, including, critically, $x \leq 0.50$, where the perovskite phase is highly stable. The detailed systematics are consistent with a first-order transformation, proceeding from the phase-pure perovskite, through perovskite−BM coexistence, to phase-pure BM. Importantly, the threshold voltage for the transformation is tunable (between ∼3 and ∼0 V) *via* Sr doping and strain, of interest for device applications. The decreasing threshold voltage with doping and strain (particularly tensile) are interpreted in terms of trends in oxygen vacancy formation enthalpy (not diffusivity), highlighting the essential role of thermodynamics (over kinetics), driven by the instability of formal Co^{4+} in these compounds. Finally, the perovskite to BM transition was shown to enable voltage control of the resistivity and Curie temperature over windows of at least 10^5 and ∼220 K, respectively. Such findings substantially advance the practical and mechanistic understanding of this voltage-driven transformation, which is emerging as paradigmatic in electrochemical gating, with fundamental and technological implications. Future work could focus on the systematics of the reverse transformation under negative gate bias, that is, electrochemical reoxidation of BM back to the perovskite $La_{1-x}Sr_xCoO_{3-\delta}$, seeking to understand reversibility, endurance, and so forth, which are critical for both fundamental understanding and applications.

■ ASSOCIATED CONTENT

Supporting Information

The Supporting Information is available free of charge at https://pubs.acs.org/doi/10.1021/acsami.1c13828.

> Evidence of long-term stability of LSCO films, additional SXRD data at various x (complementary to Figure 3b), analysis of the BM 0 0 8 to 0 0 6 SXRD intensity ratio as an indicator of BM phase purity, additional transport characterization on LSAT and SLAO substrates (complementary to Figure 2), and additional SXRD data on SLAO substrates (complementary to Figure 5b) (PDF)

■ AUTHOR INFORMATION

Corresponding Author

Chris Leighton − *Department of Chemical Engineering and Materials Science, University of Minnesota, Minneapolis, Minnesota 55455, United States;* orcid.org/0000-0003-2492-0816; Email: leighton@umn.edu

Authors

Vipul Chaturvedi − *Department of Chemical Engineering and Materials Science, University of Minnesota, Minneapolis, Minnesota 55455, United States;* orcid.org/0000-0001-6121-4756

William M. Postiglione − *Department of Chemical Engineering and Materials Science, University of Minnesota, Minneapolis, Minnesota 55455, United States*

Rohan D. Chakraborty − *Department of Chemical Engineering and Materials Science, University of Minnesota, Minneapolis, Minnesota 55455, United States*

Biqiong Yu − *School of Physics and Astronomy, University of Minnesota, Minneapolis, Minnesota 55455, United States*

Wojciech Tabiś − *School of Physics and Astronomy, University of Minnesota, Minneapolis, Minnesota 55455, United States; AGH University of Science and Technology, Faculty of Physics and Applied Computer Science, Krakow 30-059, Poland*

Sajna Hameed − *School of Physics and Astronomy, University of Minnesota, Minneapolis, Minnesota 55455, United States*

Nikolaos Biniskos − *School of Physics and Astronomy, University of Minnesota, Minneapolis, Minnesota 55455, United States*

Andrew Jacobson − *Department of Chemical Engineering and Materials Science, University of Minnesota, Minneapolis, Minnesota 55455, United States*

Zhan Zhang − *Advanced Photon Source, Argonne National Laboratory, Lemont, Illinois 60439, United States*

Hua Zhou − *Advanced Photon Source, Argonne National Laboratory, Lemont, Illinois 60439, United States;* orcid.org/0000-0001-9642-8674

Martin Greven − *School of Physics and Astronomy, University of Minnesota, Minneapolis, Minnesota 55455, United States*

Vivian E. Ferry − *Department of Chemical Engineering and Materials Science, University of Minnesota, Minneapolis, Minnesota 55455, United States;* orcid.org/0000-0002-9676-6056

Complete contact information is available at: https://pubs.acs.org/10.1021/acsami.1c13828

Author Contributions

C.L. conceived the study and oversaw its execution. V.C. deposited the films, carried out the structural characterization, and performed the transport and magnetometry measurements and analyses, collaborating with W.M.P. and A.J. under the guidance of C.L. R.D.C. performed the optical measurements and analyses, collaborating with V.C., under the guidance of V.E.F. V.C., W.M.P., B.Y., W.T., S.H., N.B., Z.Z., and H.Z. collaborated on the *operando* SXRD, under the guidance of C.L. and M.G. V.C. and C.L. wrote the paper, with input from all authors.

Notes

The authors declare no competing financial interest.

■ ACKNOWLEDGMENTS

This work was supported primarily by the National Science Foundation through the University of Minnesota MRSEC under award number DMR-2011401. Parts of this work were performed in the Characterization Facility, UMN, which receives partial support from NSF through the MRSEC and NNCI programs. Portions of this work were also conducted in the Minnesota Nano Center, which is supported by NSF through the National Nano Coordinated Infrastructure (NNCI) under ECCS-2025124. Part of this work also used resources of the Advanced Photon Source, a DOE Office of Science User Facility operated by Argonne National Laboratory under contract no. DE-AC02-06CH11357. W.T. acknowledges support from the Polish National Agency for Academic Exchange under the Polish Returns 2019 Program, grant no. PPN/PPO/2019/1/00014, and the subsidy of the Ministry of Science and Higher Education of Poland.

■ REFERENCES

(1) Leighton, C. Electrolyte-Based Ionic Control of Functional Oxides. *Nat. Mater.* **2019**, *18*, 13−18.

(2) Fujimoto, T.; Awaga, K. Electric-Double-Layer Field-Effect Transistors with Ionic Liquids. *Phys. Chem. Chem. Phys.* **2013**, *15*, 8983.

(3) Kim, S. H.; Hong, K.; Xie, W.; Lee, K. H.; Zhang, S.; Lodge, T. P.; Frisbie, C. D. Electrolyte-Gated Transistors for Organic and Printed Electronics. *Adv. Mater.* **2013**, *25*, 1822−1846.

(4) Du, H.; Lin, X.; Xu, Z.; Chu, D. Electric Double-Layer Transistors: A Review of Recent Progress. *J. Mater. Sci.* **2015**, *50*, 5641−5673.

(5) Bisri, S. Z.; Shimizu, S.; Nakano, M.; Iwasa, Y. Endeavor of Iontronics: From Fundamentals to Applications of Ion-Controlled Electronics. *Adv. Mater.* **2017**, *29*, 1607054.

(6) Xu, K.; Fullerton-Shirey, S. K. Electric-Double-Layer-Gated Transistors Based on Two-Dimensional Crystals: Recent Approaches and Advances. *J. Phys.: Mater.* **2020**, *3*, 032001.

(7) Navarro-Senent, C.; Quintana, A.; Menéndez, E.; Pellicer, E.; Sort, J. Electrolyte-Gated Magnetoelectric Actuation: Phenomenology, Materials, Mechanisms, and Prospective Applications. *APL Mater.* **2019**, *7*, 030701.

(8) Molinari, A.; Hahn, H.; Kruk, R. Voltage-Control of Magnetism in All-Solid-State and Solid/Liquid Magnetoelectric Composites. *Adv. Mater.* **2019**, *31*, 1806662.

(9) Nichterwitz, M.; Honnali, S.; Kutuzau, M.; Guo, S.; Zehner, J.; Nielsch, K.; Leistner, K. Advances in Magneto-Ionic Materials and Perspectives for Their Application. *APL Mater.* **2021**, *9*, 030903.

(10) Tan, A. J.; Huang, M.; Avci, C. O.; Büttner, F.; Mann, M.; Hu, W.; Mazzoli, C.; Wilkins, S.; Tuller, H. L.; Beach, G. S. D. Magneto-Ionic Control of Magnetism Using a Solid-State Proton Pump. *Nat. Mater.* **2019**, *18*, 35−41.

(11) Lu, N.; Zhang, P.; Zhang, Q.; Qiao, R.; He, Q.; Li, H.-B.; Wang, Y.; Guo, J.; Zhang, D.; Duan, Z.; Li, Z.; Wang, M.; Yang, S.; Yan, M.; Arenholz, E.; Zhou, S.; Yang, W.; Gu, L.; Nan, C.-W.; Wu, J.; Tokura, Y.; Yu, P. Electric-Field Control of Tri-State Phase Transformation with a Selective Dual-Ion Switch. *Nature* **2017**, *546*, 124−128.

(12) Lu, Q.; Huberman, S.; Zhang, H.; Song, Q.; Wang, J.; Vardar, G.; Hunt, A.; Waluyo, I.; Chen, G.; Yildiz, B. Bi-Directional Tuning of Thermal Transport in $SrCoO_x$ with Electrochemically Induced Phase Transitions. *Nat. Mater.* **2020**, *19*, 655−662.

(13) Lu, Q.; Yildiz, B. Voltage-Controlled Topotactic Phase Transition in Thin-Film $SrCoO_x$ Monitored by In Situ X-Ray Diffraction. *Nano Lett.* **2016**, *16*, 1186−1193.

(14) Katase, T.; Suzuki, Y.; Ohta, H. Reversibly Switchable Electromagnetic Device with Leakage-Free Electrolyte. *Adv. Electron. Mater.* **2016**, *2*, 1600044.

(15) Hu, S.; Wang, Y.; Cazorla, C.; Seidel, J. Strain-Enhanced Oxygen Dynamics and Redox Reversibility in Topotactic $SrCoO_{3-\delta}$ ($0 < \delta \leq 0.5$). *Chem. Mater.* **2017**, *29*, 708−717.

(16) Cui, B.; Song, C.; Li, F.; Zhong, X. Y.; Wang, Z. C.; Werner, P.; Gu, Y. D.; Wu, H. Q.; Saleem, M. S.; Parkin, S. S. P.; Pan, F. Electric-Field Control of Oxygen Vacancies and Magnetic Phase Transition in a Cobaltite/Manganite Bilayer. *Phys. Rev. Appl.* **2017**, *8*, 044007.

(17) Cui, B.; Werner, P.; Ma, T.; Zhong, X.; Wang, Z.; Taylor, J. M.; Zhuang, Y.; Parkin, S. S. P. Direct Imaging of Structural Changes Induced by Ionic Liquid Gating Leading to Engineered Three-Dimensional Meso-Structures. *Nat. Commun.* **2018**, *9*, 3055.

(18) Ning, S.; Zhang, Q.; Occhialini, C.; Comin, R.; Zhong, X.; Ross, C. A. Voltage Control of Magnetism above Room Temperature in Epitaxial $SrCo_{1-x}Fe_xO_{3-\delta}$. *ACS Nano* **2020**, *14*, 8949−8957.

(19) Lu, Q.; Chen, Y.; Bluhm, H.; Yildiz, B. Electronic Structure Evolution of $SrCoO_x$ during Electrochemically Driven Phase Transition Probed by *in Situ* X-Ray Spectroscopy. *J. Phys. Chem. C* **2016**, *120*, 24148−24157.

(20) Jeen, H.; Choi, W. S.; Biegalski, M. D.; Folkman, C. M.; Tung, I.-C.; Fong, D. D.; Freeland, J. W.; Shin, D.; Ohta, H.; Chisholm, M. F.; Lee, H. N. Reversible Redox Reactions in an Epitaxially Stabilized $SrCoO_x$ Oxygen Sponge. *Nat. Mater.* **2013**, *12*, 1057−1063.

(21) Long, Y.; Kaneko, Y.; Ishiwata, S.; Taguchi, Y.; Tokura, Y. Synthesis of Cubic $SrCoO_3$ Single Crystal and Its Anisotropic Magnetic and Transport Properties. *J. Phys.: Condens. Matter* **2011**, *23*, 245601.

(22) Walter, J.; Yu, G.; Yu, B.; Grutter, A.; Kirby, B.; Borchers, J.; Zhang, Z.; Zhou, H.; Birol, T.; Greven, M.; Leighton, C. Ion-Gel-Gating-Induced Oxygen Vacancy Formation in Epitaxial $La_{0.5}Sr_{0.5}CoO_{3-\delta}$ Films from *in Operando* X-ray and Neutron Scattering. *Phys. Rev. Mater.* **2017**, *1*, 071403R.

(23) De Souza, R.; Kilner, J. A. Oxygen Transport in $La_{1-x}Sr_xMn_{1-y}Co_yO_{3\pm\delta}$ Perovskites: Part I. Oxygen Tracer Diffusion. *Solid State Ionics* **1998**, *106*, 175−187.

(24) Ito, Y.; Klie, R. F.; Browning, N. D.; Mazanec, T. J. Atomic Resolution Analysis of the Defect Chemistry and Microdomain Structure of Brownmillerite-Type Strontium Cobaltite. *J. Am. Ceram. Soc.* **2004**, *85*, 969−976.

(25) Klenov, D. O.; Donner, W.; Foran, B.; Stemmer, S. Impact of Stress on Oxygen Vacancy Ordering in Epitaxial $(La_{0.5}Sr_{0.5})CoO_{3-\delta}$ Thin Films. *Appl. Phys. Lett.* **2003**, *82*, 3427−3429.

(26) Takeda, T.; Yamaguchi, Y.; Watanabe, H. Magnetic Structure of $SrCoO_{2.5}$. *J. Phys. Soc. Jpn.* **1972**, *33*, 970−972.

(27) Muñoz, A.; de la Calle, C.; Alonso, J. A.; Botta, P. M.; Pardo, V.; Baldomir, D.; Rivas, J. Crystallographic and Magnetic Structure of $SrCoO_{2.5}$ Brownmillerite: Neutron Study Coupled with Band-Structure Calculations. *Phys. Rev. B: Condens. Matter Mater. Phys.* **2008**, *78*, 054404.

(28) Gilbert, D. A.; Grutter, A. J.; Murray, P. D.; Chopdekar, R. V.; Kane, A. M.; Ionin, A. L.; Lee, M. S.; Spurgeon, S. R.; Kirby, B. J.; Maranville, B. B.; N'Diaye, A. T.; Mehta, A.; Arenholz, E.; Liu, K.; Takamura, Y.; Borchers, J. A. Ionic Tuning of Cobaltites at the Nanoscale. *Phys. Rev. Mater.* **2018**, *2*, 104402.

(29) Rippy, G.; Trinh, L.; Kane, A. M.; Ionin, A. L.; Lee, M. S.; Chopdekar, R. V.; Christiansen-Salameh, J. M.; Gilbert, D. A.; Grutter, A. J.; Murray, P. D.; Holt, M. V.; Cai, Z.; Liu, K.; Takamura, Y.; Kukreja, R. X-Ray Nanodiffraction Studies of Ionically Controlled Nanoscale Phase Separation in Cobaltites. *Phys. Rev. Mater.* **2019**, *3*, 082001R.

(30) Jonker, G. H.; Van Santen, J. H. Magnetic Compounds With Perovskite Structure III. Ferromagnetic Compounds of Cobalt. *Physica* **1953**, *19*, 120−130.

(31) Señarís-Rodríguez, M. A.; Goodenough, J. B. Magnetic and Transport Properties of the System $La_{1-x}Sr_xCoO_{3-\delta}$ ($0 < x \leq 0.50$). *J. Solid State Chem.* **1995**, *118*, 323−336.

(32) Wu, J.; Leighton, C. Glassy Ferromagnetism and Magnetic Phase Separation in $La_{1-x}Sr_xCoO_{3-\delta}$. *Phys. Rev. B: Condens. Matter Mater. Phys.* **2003**, *67*, 174408.

(33) Walter, J.; Wang, H.; Luo, B.; Frisbie, C. D.; Leighton, C. Electrostatic *versus* Electrochemical Doping and Control of Ferromagnetism in Ion-Gel-Gated Ultrathin $La_{0.5}Sr_{0.5}CoO_{3-\delta}$. *ACS Nano* **2016**, *10*, 7799−7810.

(34) Walter, J.; Charlton, T.; Ambaye, H.; Fitzsimmons, M. R.; Orth, P. P.; Fernandes, R. M.; Leighton, C. Giant Electrostatic Modification of Magnetism via Electrolyte-Gate-Induced Cluster Percolation in $La_{1-x}Sr_xCoO_{3-\delta}$. *Phys. Rev. Mater.* **2018**, *2*, 111406R.

(35) Yu, B.; Yu, G.; Walter, J.; Chaturvedi, V.; Gotchnik, J.; Hameed, S.; Freeland, J. W.; Leighton, C.; Greven, M. Soft X-Ray Absorption Spectroscopy and Magnetic Circular Dichroism as *Operando* Probes of Complex Oxide Electrolyte Gate Transistors. *Appl. Phys. Lett.* **2020**, *116*, 201905.

(36) Li, H. B.; Lou, F.; Wang, Y.; Zhang, Y.; Zhang, Q.; Wu, D.; Li, Z.; Wang, M.; Huang, T.; Lyu, Y.; Guo, J.; Chen, T.; Wu, Y.; Arenholz, E.; Lu, N.; Wang, N.; He, Q.; Gu, L.; Zhu, J.; Nan, C. W.; Zhong, X.; Xiang, H.; Yu, P. Electric Field−Controlled Multistep Proton Evolution in $H_xSrCoO_{2.5}$ with Formation of H−H Dimer. *Adv. Sci.* **2019**, *6*, 1901432.

(37) Walter, J.; Bose, S.; Cabero, M.; Yu, G.; Greven, M.; Varela, M.; Leighton, C. Perpendicular Magnetic Anisotropy via Strain-Engineered Oxygen Vacancy Ordering in Epitaxial $La_{1-x}Sr_xCoO_{3-\delta}$. *Phys. Rev. Mater.* **2018**, *2*, 111404R.

(38) Walter, J.; Bose, S.; Cabero, M.; Varela, M.; Leighton, C. Giant Anisotropic Magnetoresistance in Oxygen-Vacancy-Ordered Epitaxial $La_{0.5}Sr_{0.5}CoO_{3-\delta}$ Films. *Phys. Rev. Mater.* **2020**, *4*, 091401R.

(39) Chaturvedi, V.; Walter, J.; Paul, A.; Grutter, A.; Kirby, B.; Jeong, J. S.; Zhou, H.; Zhang, Z.; Yu, B.; Greven, M.; Mkhoyan, K. A.; Birol, T.; Leighton, C. Strain-Induced Majority Carrier Inversion in Ferromagnetic Epitaxial $LaCoO_{3-\delta}$ Thin Films. *Phys. Rev. Mater.* **2020**, *4*, 034403.

(40) Gazquez, J.; Bose, S.; Sharma, M.; Torija, M. A.; Pennycook, S. J.; Leighton, C.; Varela, M. Lattice Mismatch Accommodation via Oxygen Vacancy Ordering in Epitaxial $La_{0.5}Sr_{0.5}CoO_{3-\delta}$ Thin Films. *APL Mater.* **2013**, *1*, 012105.

(41) Torija, M. A.; Sharma, M.; Gazquez, J.; Varela, M.; He, C.; Schmitt, J.; Borchers, J. A.; Laver, M.; El-Khatib, S.; Leighton, C. Chemically Driven Nanoscopic Magnetic Phase Separation at the $SrTiO_3(001)/La_{1-x}Sr_xCoO_3$ Interface. *Adv. Mater.* **2011**, *23*, 2711−2715.

(42) Wang, H.; Walter, J.; Ganguly, K.; Yu, B.; Yu, G.; Zhang, Z.; Zhou, H.; Fu, H.; Greven, M.; Leighton, C. Wide-Voltage-Window Reversible Control of Electronic Transport in Electrolyte-Gated Epitaxial $BaSnO_3$. *Phys. Rev. Mater.* **2019**, *3*, 075001.

(43) Wang, H.; Prakash, A.; Reich, K.; Ganguly, K.; Jalan, B.; Leighton, C. Scattering Mechanisms and Mobility Enhancement in Epitaxial $BaSnO_3$ Thin Films Probed via Electrolyte Gating. *APL Mater.* **2020**, *8*, 071113.

(44) Lee, K. H.; Kang, M. S.; Zhang, S.; Gu, Y.; Lodge, T. P.; Frisbie, C. D. "Cut and Stick" Rubbery Ion Gels as High Capacitance Gate Dielectrics. *Adv. Mater.* **2012**, *24*, 4457−4462.

(45) He, C.; Eisenberg, S.; Jan, C.; Zheng, H.; Mitchell, J. F.; Leighton, C. Heat Capacity Study of Magnetoelectronic Phase Separation in $La_{1-x}Sr_xCoO_{3-\delta}$ single crystals. *Phys. Rev. B: Condens. Matter Mater. Phys.* **2009**, *80*, 214411.

(46) Cao, L.; Petracic, O.; Zakalek, P.; Weber, A.; Rücker, U.; Schubert, J.; Koutsioubas, A.; Mattauch, S.; Brückel, T. Reversible Control of Physical Properties via an Oxygen-Vacancy-Driven Topotactic Transition in Epitaxial $La_{0.7}Sr_{0.3}MnO_{3-\delta}$ Thin Films. *Adv. Mater.* **2019**, *31*, 1806183.

(47) Zhang, S.; Galli, G. Understanding the Metal-to-Insulator Transition in $La_{1-x}Sr_xCoO_{3-\delta}$ and its Applications for Neuromorphic Computing. *npj Comput. Mater.* **2020**, *6*, 170.

(48) Zhang, S.; Vo, H.; Galli, G. Predicting the Onset of Metal−Insulator Transitions in Transition Metal Oxides—A First Step in Designing Neuromorphic Devices. *Chem. Mater.* **2021**, *33*, 3187−3195.

(49) del Valle, J.; Ramírez, J. G.; Rozenberg, M. J.; Schuller, I. K. Challenges in Materials and Devices for Resistive-Switching-Based Neuromorphic Computing. *J. Appl. Phys.* **2018**, *124*, 211101.

(50) Choi, W. S.; Jeen, H.; Lee, J. H.; Seo, S. S. A.; Cooper, V. R.; Rabe, K. M.; Lee, H. N. Reversal of the Lattice Structure in $SrCoO_x$ Epitaxial Thin Films Studied by Real-Time Optical Spectroscopy and First-Principles Calculations. *Phys. Rev. Lett.* **2013**, *111*, 097401.

(51) Zhao, J.; Guo, H.; He, X.; Zhang, Q.; Gu, L.; Li, X.; Jin, K.-j.; Yang, T.; Ge, C.; Luo, Y.; He, M.; Long, Y.; Wang, J.-o.; Qian, H.; Wang, C.; Lu, H.; Yang, G.; Ibrahim, K. Manipulating the Structural and Electronic Properties of Epitaxial $SrCoO_{2.5}$ Thin Films by Tuning the Epitaxial Strain. *ACS Appl. Mater. Interfaces* **2018**, *10*, 10211−10219.

(52) Youssef, M.; Van Vliet, K. J.; Yildiz, B. Polarizing Oxygen Vacancies in Insulating Metal Oxides under a High Electric Field. *Phys. Rev. Lett.* **2017**, *119*, 126002.

(53) Mizusaki, J.; Mima, Y.; Yamauchi, S.; Fueki, K.; Tagawa, H. Nonstoichiometry of the Perovskite-Type Oxides $La_{1-x}Sr_xCoO_{3-\delta}$. *J. Solid State Chem.* **1989**, *80*, 102−111.

(54) Curnan, M. T.; Kitchin, J. R. Effects of Concentration, Crystal Structure, Magnetism, and Electronic Structure Method on First-Principles Oxygen Vacancy Formation Energy Trends in Perovskites. *J. Phys. Chem. C* **2014**, *118*, 28776−28790.

(55) Jia, T.; Zeng, Z.; Zhang, X.; Ohodnicki, P.; Chorpening, B.; Hackett, G.; Lekse, J.; Duan, Y. The Influence of Oxygen Vacancy on the Electronic and Optical Properties of $ABO_{3-\delta}$ (A = La, Sr, B = Fe, Co) Perovskites. *Phys. Chem. Chem. Phys.* **2019**, *21*, 20454−20462.

(56) Deml, A. M.; Stevanović, V.; Muhich, C. L.; Musgrave, C. B.; O'Hayre, R. Oxide Enthalpy of Formation and Band Gap Energy as Accurate Descriptors of Oxygen Vacancy Formation Energetics. *Energy Environ. Sci.* **2014**, *7*, 1996−2004.

(57) Tahini, H. A.; Tan, X.; Schwingenschlögl, U.; Smith, S. C. Formation and Migration of Oxygen Vacancies in $SrCoO_3$ and Their Effect on Oxygen Evolution Reactions. *ACS Catal.* **2016**, *6*, 5565−5570.

(58) Donner, W.; Chen, C.; Liu, M.; Jacobson, A. J.; Lee, Y.-L.; Gadre, M.; Morgan, D. Epitaxial Strain-Induced Chemical Ordering in $La_{0.5}Sr_{0.5}CoO_{3-\delta}$ Films on $SrTiO_3$. *Chem. Mater.* **2011**, *23*, 984−988.

(59) Mefford, J. T.; Rong, X.; Abakumov, A. M.; Hardin, W. G.; Dai, S.; Kolpak, A. M.; Johnston, K. P.; Stevenson, K. J. Water Electrolysis on $La_{1-x}Sr_xCoO_{3-\delta}$ Perovskite Electrocatalysts. *Nat. Commun.* **2016**, *7*, 11053.

(60) Pan, Y.; Xu, X.; Zhong, Y.; Ge, L.; Chen, Y.; Veder, J.-P. M.; Guan, D.; O'Hayre, R.; Li, M.; Wang, G.; Wang, H.; Zhou, W.; Shao, Z. Direct Evidence of Boosted Oxygen Evolution over Perovskite by Enhanced Lattice Oxygen Participation. *Nat. Commun.* **2020**, *11*, 2002.

(61) Takeda, Y.; Kanno, R.; Takada, T.; Yamamoto, O.; Takano, M.; Bando, Y. Phase Relation and Oxygen-Non-Stoichiometry of Perovskite-like Compound $SrCoO_x$ ($2.29 < x < 2.80$). *Z. Anorg. Allg. Chem.* **1986**, *540*, 259−270.

(62) Van Buren, F. R.; Broers, G. H. J.; Bouman, A. J.; Boesveld, C. The Electrochemical Determination of Oxygen Ion Diffusion Coefficients in $La_{0.5}Sr_{0.5}CoO_{3-y}$. *J. Electroanal. Chem. Interfacial Electrochem.* **1978**, *88*, 353−361.

https://doi.org/10.1021/acsami.1c13828